improved room-temperature dielectric constant.

The dielectric properties of the composites under different applied-field strength were characterized by directly measuring the magnitude and the phase of the current passing through the composite under a given a.c. voltage. From the complex electric impedance $Z^* = 1/(j\omega C^*)$ and $C^* = (K' - jK'')\varepsilon_0 A/t$, both the real and imaginary parts (K' and K'') of the dielectric constant can be determined, where A is the area and t is the thickness of the capacitor, and ω is the angular frequency. The elastic modulus was determined using a commercial dynamic mechanical analyser (TA Instruments, DMA2980). The electric-field-induced strain along the applied-field direction (longitudinal strain) was measured using a piezobimorph-based sensor[30].

Received 18 April; accepted 25 July 2002; doi:10.1038/nature01021.

1. Bar-Cohen, Y. (ed.) *Electroactive Polymer Actuators as Artificial Muscles* (SPIE, Bellingham, WA, 2001).
2. Zhang, Q. M., Furukawa, T., Bar-Cohen, Y. & Scheinbeim, J. (eds) *Electroactive Polymers* (MRS Symp. Proc. Vol. 600, MRS, Warrendale PA, 1999).
3. Nalwa, H. (ed.) *Ferroelectric Polymers* (Marcel Dekker, New York, 1995).
4. Zhang, Q. M., Bharti, V. & Zhao, X. Giant electrostriction and relaxor ferroelectric behavior in electron-irradiated poly(vinylidene fluoride-trifluofoethylene) copolymer. *Science* **280,** 2101–2104 (1998).
5. Pelrine, R., Kornbluh, R., Pei, Q. & Joseph, J. Highspeed electrically actuated elastomers with strain greater than 100%. *Science* **287,** 836–839 (2000).
6. Lehmann, W. *et al.* Giant lateral electrostriction in ferroelectric liquid-crystalline elastomers. *Nature* **410,** 447–450 (2001).
7. Baughman, R. H. *et al.* Carbon nanotube actuators. *Science* **284,** 1340–1344 (1999).
8. Osada, Y., Okuzaki, H. & Hori, H. A polymer gel with electrically driven motility. *Nature* **355,** 242–244 (1992).
9. Cheng, Z.-Y. *et al.* Electrostrictive poly(vinylidene fluoride-trifluoroethylene) copolymers. *Sens. Actuat. A* **90,** 138–147 (2001).
10. Xu, H. *et al.* Ferroelectric and electromechanical properties of poly(vinylidene-fluoride–trifluoroethylene–cholorotrifluoroethylene) terpolymer. *Appl. Phys. Lett.* **78,** 2360–2362 (2001).
11. Huber, J. E., Fleck, N. A. & Ashby, M. F. The selection of mechanical actuators based on performance indices. *Proc. R. Soc. Lond. A* **453,** 2185–2205 (1997).
12. Dario, P., Carrozza, M., Benvenuto, A. & Menciassi, A. Micro-systems in biomedical applications. *J. Micromech. Microeng.* **10,** 235–244 (2000).
13. McCrum, N., Read, B. E. & Williams, G. *Anelastic and Dielectric Effects in Polymeric Solids* (Dover, New York, 1967).
14. Moulson, A. & Herbert, J. *Electroceramics* (Chapman & Hall, London, 1995).
15. Cross, L. E. Ferroelectric ceramics: materials and application issues. *Ceram. Trans.* **68,** 15–55 (1996).
16. Safari, A., Sa-gong, G., Giniewicz, J. & Newnham, R. Composite piezoelectric sensors. *Proc. 21st Univ. Conf. Ceram. Sci.* **20,** 445–455 (1986).
17. Bao, Z., Lovinger, A. & Dodabalapur, A. Highly ordered vacuum-deposited thin films of metallophthalocyanines and their application in field-effect transistors. *Adv. Mater.* **9,** 42–45 (1997).
18. Tominaga, T., Hayashi, K. & Toshima, N. Accelerated hole transfer by double-layered metallophthalocyanine thin film for effective electroluminescence. *Appl. Phys. Lett.* **70,** 762–763 (1997).
19. Nalwa, H. S., Dalton, L. & Vasudevan, P. Dielectric properties of copper-phthalocyanine polymer. *Eur. Polym. J.* **21,** 943–947 (1985).
20. Phougat, N., Vasudevan, P. & Nalwa, H. *Handbook of Low and High Dielectric Constant of Materials and Their Applications* Ch. 8 (ed. Nalwa, H.)) (Academic, London, 1999).
21. Vijayakumar, P. & Pohl, H. A. Giant polarization in stable polymeric dielectrics. *J. Polym. Sci. Poly. Phys.* **22,** 1439–1451 (1984).
22. Gould, P. D. Structure and electrical conduction properties of phthalocyanine thin films. *Coord. Chem. Rev.* **156,** 237–274 (1996).
23. Landau, L. D. & Lifshitz, E. M. *Electrodynamics of Continuous Media* (Pergamon, Oxford, 1970).
24. Newnham, R., Sundar, V., Yimmirun, R., Su, J. & Zhang, Q. M. Electrostriction in dielectric materials. *Ceram. Trans.* **88,** 15–39 (1998).
25. Damjanovic, D. Logarithmic frequency dependence of the piezoelectric effect due to pinning of ferroelectric-ferroelastic domain walls. *Phys. Rev. B* **55,** R649–R652 (1997).
26. Su, J., Zhang, Q. M. & Ting, R. Y. Space-charge-enhanced electromechanical response in thin-film polyurethane elastomers. *Appl. Phys. Lett.* **71,** 386–388 (1997).
27. Hayashi, K., Kawato, S., Fujii, Y., Horiuchi, T. & Matsushige, K. Effect of applied electric field on the molecular orientation of epitaxially grown organic films. *Appl. Phys. Lett.* **70,** 1384–1386 (1997).
28. Ai-Aliak, H., Illingsworth, J., Brinkman, A., Russell, G. J. & Woods, J. The effects of donor dopant concentration on the grain boundary layer characteristics in *n*-doped $BaTiO_3$ ceramics. *J. Appl. Phys.* **64,** 6477–6482 (1998).
29. Achar, B. N., Fohlen, G. G. & Parker, J. A. Phthalocyanine polymers. II Synthesis and characterization of some metal phthalocyanine sheet oligomers. *J. Polym. Sci. Polym. Chem.* **20,** 1785–1790 (1982).
30. Su, J., Moses, P. & Zhang, Q. M. A piezoelectric bimorph based dilatometer for field induced strain measurement in soft and thin free standing polymer films. *Rev. Sci. Instrum.* **69,** 2480–2484 (1998).

Acknowledgements

This work was supported by the National Institutes of Health, the Office of Naval Research, and Defense Advanced Research Projects Agency.

Competing interests statement

The authors declare that they have no competing financial interests.

Correspondence and requests for materials should be addressed to Q.M.Z. (e-mail: qxz1@psu.edu).

Testing time-predictable earthquake recurrence by direct measurement of strain accumulation and release

Jessica Murray & Paul Segall

Geophysics Department, Stanford University, Stanford, California 94305-2215, USA

Probabilistic estimates of earthquake hazard use various models for the temporal distribution of earthquakes, including the 'time-predictable' recurrence model formulated by Shimazaki and Nakata[1] (which incorporates the concept of elastic rebound described as early as 1910 by H. F. Reid[2]). This model states that an earthquake occurs when the fault recovers the stress relieved in the most recent earthquake. Unlike time-independent models (for example, Poisson probability), the time-predictable model is thought to encompass some of the physics behind the earthquake cycle, in that earthquake probability increases with time. The time-predictable model is therefore often preferred when adequate data are available, and it is incorporated in hazard predictions for many earthquake-prone regions, including northern California[3], southern California[4,5], New Zealand[6] and Japan[7]. Here we show that the model fails in what should be an ideal locale for its application — Parkfield, California. We estimate rigorous bounds on the predicted recurrence time of the magnitude ~6 1966 Parkfield earthquake through inversion of geodetic measurements and we show that, according to the time-predictable model, another earthquake should have occurred by 1987. The model's poor performance in a relatively simple tectonic setting does not bode well for its successful application to the many areas of the world characterized by complex fault interactions.

The time-predictable model states that the time to the next earthquake is the stress drop in the most recent earthquake divided by the fault stressing-rate. Although stress is difficult to measure *in situ*, the Earth's crust is linearly elastic, so strain is proportional to stress[8]. Geodetic measurements may be used to estimate both the strain released in an earthquake and the interseismic strain rate. If we can use such estimates to show with a high degree of confidence that the strain released in the most recent earthquake has already accumulated without a subsequent earthquake, then the time-predictable model has failed.

The Parkfield segment of the San Andreas fault (Fig. 1a) is a natural choice for a test of the time-predictable model. At least five historic earthquakes of $M \approx 6$ have occurred in this area, most recently in 1966. The average time between earthquakes is about 22 years. The three latest events had striking similarities[9], including comparable seismic moment and epicentral location. Inferred epicentres for the older events, although uncertain, are consistent with this location. The absence of active sub-parallel faults in this section of the San Andreas system makes Parkfield a particularly good place to test the time-predictable model. This test is possible because geodetic data have been collected here for over 40 yr (refs 10–12), making Parkfield one of the few places where strain has been measured for times exceeding the average inter-event time.

Inversion of geodetic data collected since 1966 has shown that although the San Andreas exhibits shallow creep near Parkfield, the fault is either locked or slowly slipping at depth[12–14] (see Fig. 1b). This demonstrates that strain has been accumulating throughout what has now become the longest recorded interseismic period for $M \approx 6$ earthquakes at Parkfield.

The coseismic moment, a measure of strain release, is given by

$$M_o = \mu \int\int_A s\mathrm{d}A \quad (1)$$

where μ is the shear modulus, A is the area that slipped, and s is the (spatially variable) amount of slip. We approximate the complex interseismic loading of the seismogenic zone by aseismic slip at a constant rate on a downward extension of the fault[15]. If the seismogenic fault were slipping everywhere at this long-term deep slip-rate, no strain would accumulate. With a spatially variable slip-rate, however, some parts of the fault experience a slip deficit relative to the long-term slip-rate. The moment deficit rate is

$$\dot{M}_d = \mu \int\int_A (\dot{s}_\infty - \dot{s})\mathrm{d}A \quad (2)$$

where $\dot{s}_\infty$ is the long-term deep slip-rate, $\dot{s}$ the (spatially variable) slip-rate, and $\dot{s}_\infty - \dot{s}$ the slip deficit rate. The time-predictable inter-event time, t_i, can be written as:

$$t_i = M_o/\dot{M}_d \quad (3)$$

Given certain assumptions about the fault stress[8], t_i measures the time required for elastic strain energy to recover in the crustal volume surrounding the fault.

We used two geodetic data sets: (1) trilateration measurements of the distances between benchmarks[11]; and (2) global positioning system (GPS) estimates of benchmark positions[12]. Trilateration measurements repeated over time can be used to estimate rates of distance change, whereas GPS measurements over time produce velocities of individual stations (Fig. 1a). We inverted these data for the slip distribution of the 1966 earthquake and the slip-rate distribution for the interseismic period (1966 to 1998), from which the coseismic moment (M_o) and interseismic moment deficit rate ($\dot{M}_d$) can be derived.

These inversions require the choice of a model fault geometry (Fig. 1), one component of which is a transition depth below which

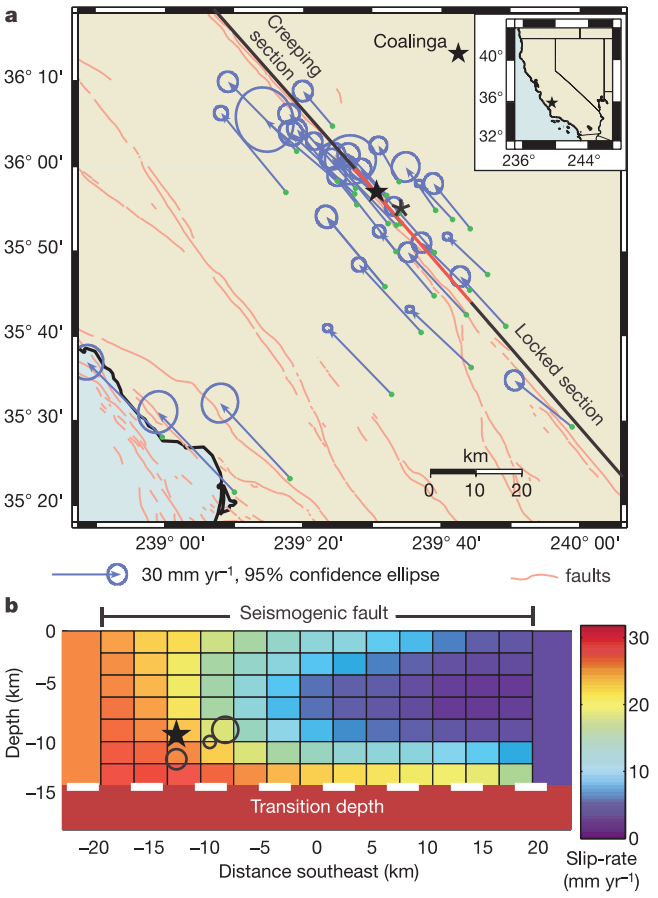

Figure 1 Parkfield segment of the San Andreas fault. The unlabelled stars on **a** and **b** represent the 1966 earthquake. **a**, The San Andreas fault near the town of Parkfield (asterisk) forms a transition between the creeping segment to the northwest and the locked section to the southeast. Vectors indicate GPS velocities (1991–1998) relative to North America. Black and red line is model fault trace; red portion is the seismogenic fault which is divided into subfaults (dislocations). **b**, Slip-rate estimated for each subfault after Murray *et al.*[12] Zero on *x*-axis is the midpoint of seismogenic fault in **a**. The northwestern endpoint is at 36° N, 239° 27′ E; the southeastern endpoint is at 35° 44′ N, 239° 44′ E. Circles are earthquakes occurring in (from northwest to southeast) November 1993 ($M = 4.6$), October 1992 ($M = 4.3$) and December 1994 ($M = 4.7$). Area of circles is equivalent to the rupture area of a 3 MPa stress drop crack[30].

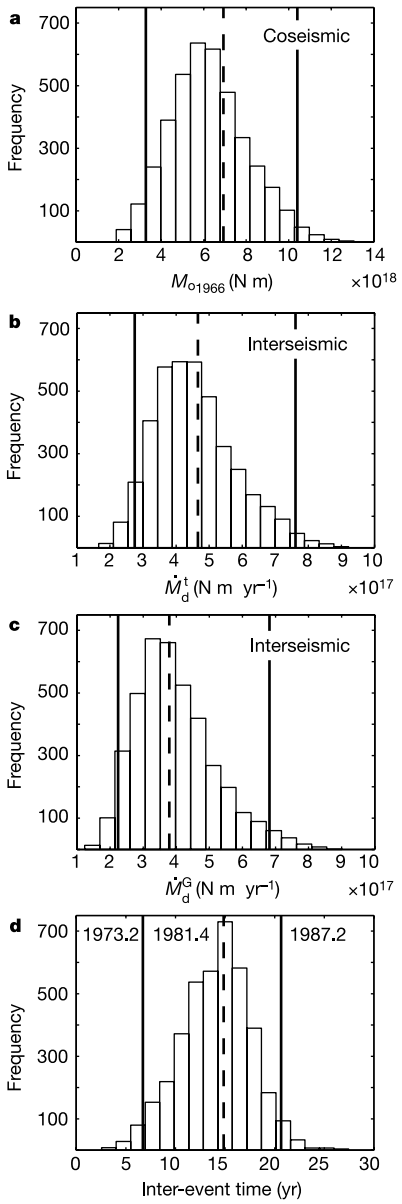

Figure 2 Bootstrap distributions for moment, moment deficit rate, and inter-event time. 95% confidence bounds are indicated by the solid lines. **a**, Coseismic M_o, lower bound is 3.3×10^{18} N m and upper bound is 1.0×10^{19} N m. **b**, Interseismic $\dot{M}_d$ found using trilateration data, 2.7×10^{17} N m yr^{-1} to 7.6×10^{17} N m yr^{-1}. **c**, Interseismic $\dot{M}_d$ found using GPS data, 2.2×10^{17} N m yr^{-1} to 6.8×10^{17} N m yr^{-1}. **d**, Predicted inter-event time, 6.7–20.7 yr. Dashed lines indicate best-fitting value using the original (not resampled) data set.

the fault is assumed to slip aseismically at the long-term rate. There is a well-known trade-off between the estimated transition depth and deep slip-rate; the greater the transition depth the higher is the deep slip-rate[12,13]. Another complication is that inversion of geodetic data for fault slip is not unique. Regularizing the inversion by, for example, imposing spatial smoothing as in Fig. 1b, produces results contingent on this assumption.

Using data up to 1984, Segall and Harris[8] found inter-event times from 5 to 29 years. Their analysis was restricted to regularized inversions, and they did not develop a probability distribution of recurrence times. We have analysed nearly twice as much data consisting of (1) coseismic line-length changes, (2) interseismic rates of line-length change (1966–1991), and (3) GPS velocities (1991–1998). We followed Johnson *et al.*[16] and employed constrained inversion to determine M_o and $\dot{M}_d$ independently of assumptions such as smoothness. Bootstrap methods[17] were used to incorporate uncertainty in the transition depth and deep slip-rate and to produce distributions of M_o and of $\dot{M}_d$ from which we determined rigorous bounds on inter-event time.

The range of coseismic M_o at 95% confidence, 3.3×10^{18} N m to 1.0×10^{19} N m (moment magnitude, M_w, of 6.3–6.6), estimated from the bootstrap resamples (Fig. 2a), is consistent with other estimates based on geodetic data[8,18], but larger than that found using surface waves[19] (0.9×10^{18} to 2.1×10^{18} N m). The trilateration data spanning the earthquake were collected fairly close to the fault, allowing large slip at depth without causing large misfit to the data (Fig. 3a). Moreover, considerable afterslip was observed following this event[20]. Because we are interested in the time needed to accumulate the total moment associated with this earthquake, it is irrelevant whether the slip occurred during fast rupture or post-seismic transient. The $\dot{M}_d$ estimated from the trilateration and GPS data sets individually are comparable, with slightly greater values found using the trilateration data (Fig. 2b, c). The resulting bounds on inter-event time (Fig. 2d) range from 7 to 21 years at 95% confidence. In other words, the strain released in 1966 recovered some time between 1973 and 1987. The expected earthquake has yet to occur.

There are several possible explanations for the time-predictable model's inability to predict the $M \approx 6$ Parkfield earthquake. The model assumes that an earthquake occurs when the fault reaches a critical stress. However, local variations in pore fluid pressure could modulate the stress required for earthquake nucleation. Moreover, formulations for fault failure such as rate and state friction do not embody a characteristic failure stress. Rather, acceleration toward unstable slip depends on the elastic loading system, frictional properties of the fault, and past slip history[21,22]. Stress perturbations may lead to evolution of the fault 'state', thus affecting the time to the next earthquake[23]. For example, Simpson *et al.*[24] showed that static stress changes due to the Coalinga earthquake of 1983 may have delayed the next $M \approx 6$ Parkfield earthquake by 1 or 2 years. Including rate and state effects, this delay could extend into the mid-1990s but cannot explain the now 36-year-long quiescence[25]. Simple stress-change calculations suggest that three $M \geq 4.3$ earthquakes that occurred near the 1966 hypocentre between 1992 and 1994 (Fig. 1b) increased stress at the 1966 hypocentre, countering the effects of the Coalinga quake. There is also evidence for a change in strain rate in the early to mid-1990s (ref. 26).

There may also be a much longer scale decrease in stressing rate following the 1857 Fort Tejon earthquake, which has led to the suggestion that the recurrence times of Parkfield earthquakes should increase with time[27]. That the recent GPS data predict a deep slip-rate consistent with the geologic rate[12], however, suggests that transient effects due to the 1857 event are currently small. Furthermore, in this study we used actual measurements of strain accumulation post-1966, and our conclusions are independent of longer-term variations in loading. The consistency between GPS and geologically derived deep slip-rates also suggests that any inelastic component of the measured strain is small.

The time-predictable model as conceived by Shimazaki and Nakata[1], and as applied in hazard assessment, assumes repeated rupture of the same fault segment. The 1934 Parkfield earthquake

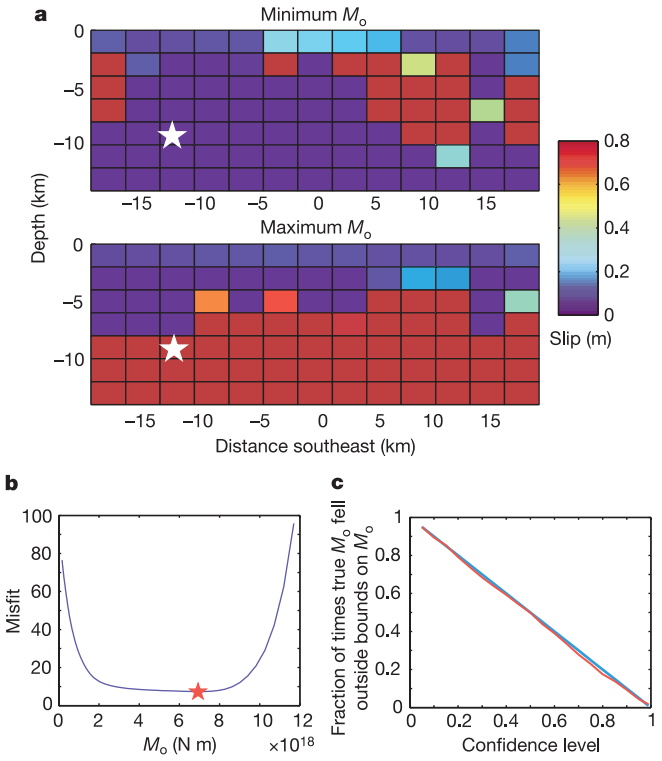

Figure 3 Constrained inversion and bootstrap procedure. **a**, Slip distributions from constrained inversion corresponding to 95% confidence limits on M_o for transition depth of 14 km. The fault plane is same as the gridded plane in Fig. 1b; the star is 1966 hypocentre. For the minimum M_o (3.2×10^{18} N m), the inversion results have most slip at the southeastern end of the fault where the geodetic measurements were concentrated. For the maximum M_o (7.9×10^{18} N m), the results have considerable slip at depth and at the northwestern end where data resolution was poor. **b**, Misfit ($\mathbf{r}^T\Sigma^{-1}\mathbf{r}$) as a function of coseismic M_o. **r** is the difference between observed and predicted data, and Σ is the data covariance. **c**, Test of the constrained inversion/bootstrap method for bounding M_o using synthetic data; blue line is predicted behaviour, red line is observed behaviour.

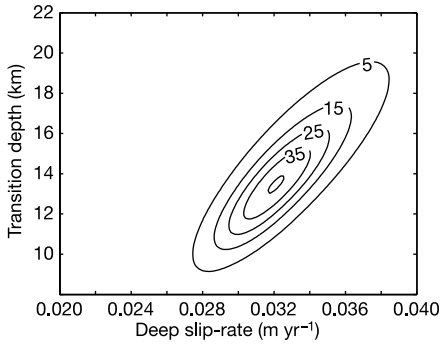

Figure 4 Approximate joint probability density function (indicated on contours) for transition depth and deep slip-rate. The PDF is proportional to e^{-CVSS} (see text) and normalized so that the volume under the surface is one; we note the strong positive correlation between slip-rate and transition depth.

probably ruptured a shorter segment than that in 1966 (ref. 18). However, repeating our test using only estimates of 1966 strain release and subsequent accumulation on the inferred 1934 rupture segment results in nearly identical predicted recurrence times.

Although the time-predictable model does not require successive earthquakes to be of constant size, hazard assessments generally concern the repeat of large earthquakes. The $M \geq 4.3$ earthquakes between 1992 and 1994 were not considered sufficient to fulfill the Parkfield prediction, nor did they rupture the same area as the 1966 quake. These events may indicate that the stress released in 1966 had reaccumulated near the hypocentre by the early 1990s. However, the local stress may depend on details of the creep distribution, so these events do not constrain the stress averaged over the Parkfield segment. The $M = 4.6$ earthquake in 1993 was similar to a foreshock of the 1934 $M \approx 6$ earthquake[28]. That no $M \approx 6$ event occurred in the early 1990s suggests that conditions for unstable slip may be met locally on the fault, but the earthquake's ultimate size depends on detailed stress distribution and complex rupture dynamics.

Another recurrence model, the slip-predictable model[1], posits that the slip in the next earthquake equals the accumulated slip deficit. This model, which incorporates assumptions similar to those of the time-predictable model (for example, representing earthquakes by only moment and time), cannot be tested until the next $M > 6$ Parkfield quake. However given the current slip deficit rate, were an earthquake to occur on the 1966 rupture plane in 2002 the slip predictable model would require a moment of 9.2×10^{18} N m to 2.6×10^{19} N m ($M_w = 6.6$–6.9), considerably larger than the 1966 earthquake.

That the time-predictable model does not accurately predict the anticipated $M \approx 6$ earthquake at Parkfield indicates that there are crucial aspects of earthquake physics, even in a fairly simple and well-understood setting, that this model does not capture. It would be useful to apply the methods developed here to other faults, although to date few have the required history of geodetic observations. Newly developed GPS networks will provide the measurements necessary to determine if Parkfield is representative of the majority of active fault segments. □

Methods

Constrained inversion

Constrained inversion involves finding the slip (or slip deficit rate) distribution that best fits the data, subject to the constraint that the seismic moment (or moment deficit rate) equals a specified value. The model fault (Fig. 1) was based on the mapped fault trace and seismicity[12]. Measured surface offsets from the 1966 event were used to bound the estimated coseismic slip in subfaults that break the earth's surface[20]. Shallow creep rates inferred from near-fault monitoring instruments were used to bound the slip-rates on these subfaults in the inversions for interseismic slip deficit rate[13]. For the interseismic period, the contribution to line-length rate of change or GPS velocity from slip on the creeping section of the San Andreas and from slip below the transition depth were incorporated with uniformly slipping dislocations[12] (note that these dislocations are larger than shown in Fig. 1b). We constrained slip to be positive (right lateral), but made no assumption of smoothness (for example, see Fig. 3a). The upper bound for coseismic slip was 0.8 m, which exceeds the maximum slip estimated in previous studies[8,18]. The maximum allowable slip deficit rate was the deep slip-rate. We swept through a range of moments and found a best-fitting solution for each one (Fig. 3b). The M_o with the lowest misfit (star in Fig. 3b) is optimal in the sense that there are no slip distributions resulting in different moments that fit the data better.

The bootstrap

The range of moments that fit the data acceptably well is more important than the best-fitting M_o. To identify this range, we used the bootstrap, which involves resampling the data a large number of times and repeating the inversions with each resampled data set, resulting in many realizations of the estimated quantity. We repeated the constrained inversions for best-fitting M_o 4,000 times, yielding a distribution of M_o estimates, and did the same for the interseismic period to infer the distribution of $\dot{M}_d$. We then used these distributions in the calculation for inter-event time.

The distributions can also be used to obtain confidence intervals on M_o and $\dot{M}_d$. We found this method for inferring the range of M_o that fit the data to be successful in an empirical test using data predicted from a hypothetical slip distribution (Fig. 3c). We repeated the constrained inversion and bootstrap process 700 times with different random errors added to the synthetic data. The fraction of times the 'true' M_o fell outside the inferred range is shown as a function of confidence interval (Fig. 3c, red line). For comparison, the blue line shows the predicted behaviour; for example, at the 95% confidence level the 'true' M_o should fall outside the range 5% of the time.

Uncertainty in transition depth and deep slip-rate

The estimates of M_o and $\dot{M}_d$ resulting from the constrained inversion and bootstrap are conditional on an assumed transition depth, and in the case of $\dot{M}_d$, deep slip-rate. Although the geodetic data provide some constraints on these parameters, they are not uniquely resolved. Murray *et al.*[12] estimated interseismic slip-rates for a range of transition depth and deep slip-rate pairs with optimal smoothing determined by cross-validation[29]. The cross validation sum of squares (CVSS), a measure of misfit, is a nearly quadratic function of transition depth and deep slip-rate. Its minimum is at 14 km and 33 mm yr^{-1}, in keeping with independent geologic and seismic observations. For linear least squares the residual sum of squares (RSS) is quadratic, and the corresponding probability density function (PDF) is proportional to $e^{-\mathrm{RSS}}$. We used the observed distribution of CVSS to generate an approximate PDF proportional to $e^{-\mathrm{CVSS}}$ (Fig. 4). Each time the data were resampled in the bootstrap, a new transition depth and deep slip-rate pair was chosen from this empirical distribution.

Calculating inter-event time

The distribution for interevent time (Fig. 2d) was calculated from the ratios of M_o to $\dot{M}_d$, ensuring that for each pair of M_o and $\dot{M}_d$ both were found using the same transition depth. Noting that we had 25 years of trilateration measurements without a Parkfield earthquake, we estimate the inter-event time as:

$$\Delta t = \frac{M_{o_{1966}}}{\dot{M}_d^t} \tag{4}$$

if $M_{o_{1966}} - (\dot{M}_d^t \times 25\,\mathrm{yr}) \leq 0$, and

$$\Delta t = 25\,\mathrm{yr} + \frac{M_{o_{1966}} - (\dot{M}_d^t \times 25\,\mathrm{yr})}{\dot{M}_d^G} \tag{5}$$

if $M_{o_{1966}} - (\dot{M}_d^t \times 25\,\mathrm{yr}) > 0$ where the next earthquake is predicted to occur in $1966 + \Delta t$. $M_{o_{1966}}$ is the coseismic moment, $\dot{M}_d^t$ is the moment deficit rate inferred from trilateration data, and $\dot{M}_d^G$ is that inferred from GPS data.

Received 5 March; accepted 15 July 2002; doi:10.1038/nature00984.

1. Shimazaki, K. & Nakata, T. Time-predictable recurrence model for large earthquakes. *Geophys. Res. Lett.* **7,** 279–282 (1980).
2. Reid, H. F. *The California Earthquake of April 18, 1906* Report of the state earthquake investigation commission Vol. 2 (Carnegie Institute, Washington DC, 1910).
3. Working Group on California Earthquake Probabilities *Earthquake probabilities in the San Francisco Bay Region: 2000 to 2030 – A summary of findings* US Geological Survey open-file report 99-517 (USGS, Reston, VA, 1999).
4. Working Group on California Earthquake Probabilities Seismic hazards in southern California: probable earthquakes, 1994 to 2024. *Bull. Seismol. Soc. Am.* **85,** 379–439 (1995).
5. Cramer, C. H., Petersen, M. D., Tianqing, C., Toppozada, T. R. & Reichle, M. A time-dependent probabilistic seismic-hazard model for California. *Bull. Seismol. Soc. Am.* **90,** 1–21 (2000).
6. Stirling, M. W. *Proc. 12th World Conference on Earthquake Engineering* (New Zealand Society for Earthquake Engineering, Pergamon, Oxford, 2000).
7. Annaka, T. & Yashiro, H. *Risk Analysis* (eds Rubio, J. L.Brebbia, C. A. and Uso, J-L.) (WIT Press, Boston, 1998).
8. Segall, P. & Harris, R. Earthquakes deformation cycle on the San Andreas fault near Parkfield, California. *J. Geophys. Res.* **92,** 10511–10525 (1987).
9. Bakun, W. H. & McEvilly, T. V. Recurrence models and Parkfield, California, earthquakes. *J. Geophys. Res.* **89,** 3051–3058 (1984).
10. Roeloffs, E. & Langbein, J. The earthquake prediction experiment at Parkfield, California. *Rev. Geophys.* **32,** 315–336 (1994).
11. King, N. E., Segall, P. & Prescott, W. Geodetic measurements near Parkfield, California, 1959-1984. *J. Geophys. Res.* **92,** 2747–2766 (1987).
12. Murray, J. R., Segall, P., Cervelli, P., Prescott, W. & Svare, J. Inversion of GPS data for spatially variable slip-rate on the San Andreas fault near Parkfield, CA. *Geophys. Res. Lett.* **28,** 359–362 (2001).
13. Harris, R. A. & Segall, P. Detection of a locked zone at depth on the Parkfield, California, segment of the San Andreas fault. *J. Geophys. Res.* **92,** 7945–7962 (1987).
14. Snay, R. A. Enhancing the geodetic resolution of fault slip by introducing prior information. *Manuscr. Geodetica* **14,** 391–403 (1989).
15. Savage, J. C. Equivalent strike-slip earthquake cycles in half-space and lithosphere-asthenosphere Earth models. *J. Geophys. Res.* **95,** 4873–4879 (1990).
16. Johnson, H. O., Agnew, D. C. & Hudnut, K. Extremal bounds on earthquake movement from geodetic data: Application to the Landers earthquake. *Bull. Seismol. Soc. Am.* **84,** 660–667 (1994).
17. Efron, B. & Tibshirani, R. J. *An Introduction to the Bootstrap: Monographs on Statistics and Applied Probability 57* (Chapman and Hall, New York, 1993).
18. Segall, P. & Du, Y. How similar were the 1934 and 1966 Parkfield earthquakes? *J. Geophys. Res.* **98,** 4527–4538 (1993).
19. Tsai, Y.-B. & Aki, K. Simultaneous determination of the seismic moment and attenuation of seismic surface waves. *Bull. Seismol. Soc. Am.* **59,** 275–287 (1969).
20. Smith, S. W. & Wyss, M. Displacement on the San Andreas fault subsequent to the 1966 Parkfield earthquake. *Bull. Seismol. Soc. Am.* **58,** 1955–1973 (1968).
21. Rice, J. R. & Ruina, A. L. Stability of steady frictional sliding. *J. Appl. Mech. Trans. ASME* **50,** 343–349 (1983).
22. Dieterich, J. & Kilgore, B. Implications of fault constitutive properties for earthquake prediction. *Proc. Natl Acad. Sci. USA* **93,** 3787–3794 (1996).
23. Dieterich, J. A constitutive law for rate of earthquake production and its application to earthquake clustering. *J. Geophys. Res.* **99,** 2601–2618 (1994).
24. Simpson, R. W., Schulz, S. S., Dietz, L. D. & Burford, R. O. The response of creeping parts of the

San Andreas Fault to earthquakes on nearby faults: Two examples. *Pure Appl. Geophys.* **126,** 665–685 (1988).
25. Toda, S. & Stein, R. Response of the San Andreas fault to the 1983 Coalinga-Nuñez earthquakes: An application of interaction-based probabilities for Parkfield. *J. Geophys. Res.* **107,** 10.1029/2001 JB000172, 2002.
26. Gao, S., Silver, P. G. & Linde, A. T. Analysis of deformation data at Parkfield, California: Detection of a long-term strain transient. *J. Geophys. Res.* **105,** 2955–2967 (2000).
27. Ben-Zion, Y., Rice, J. R. & Dmowska, R. Interaction of the San Andreas fault creeping segment with adjacent great rupture zones and earthquake recurrence at Parkfield. *J. Geophys. Res.* **98,** 2135–2144 (1993).
28. Cole, A. T. & Ellsworth, W. L. Earthquake clustering and the long-term evolution of seismicity near Parkfield, California, 1931-1994. *Seismol. Res. Lett.* **66,** 28 (1995).
29. Wahba, G. *Spline Models for Observational Data* (Society for Industrial and Applied Mathematics, Philadelphia, 1990).
30. Ellsworth, W., Waldhauser, F. & Cole, A. A new view of the San Andreas Fault: Implications for earthquake interaction at Parkfield. Extended abstract for the 17th Course of the International School of Geophysics "Fault Interaction by Stress Transfer: New Horizons for Understanding Earthquake Occurrence", Ettore Majorana Foundation and Centre for Scientific Culture, Erice, Italy, 17–23 June 2000.

Acknowledgements

We thank P. Cervelli, J. Savage, R. Tibshirani, J. Langbein, W. Prescott, J. Svarc and H. Johnson for comments and advice. Funding was provided by Stanford University Graduate Fellowships and a USGS National Earthquake Hazards Reduction Program grant.

Competing interests statement

The authors declare that they have no competing financial interests.

Correspondence and requests for materials should be addressed to J.M. (e-mail: jrmurray@pangea.stanford.edu).

An unusual oviraptorosaurian dinosaur from China

Xing Xu*, Yen-Nien Cheng†, Xiao-Lin Wang* & Chun-Hsiang Chang†

** Institute of Vertebrate Paleontology & Paleoanthropology, Chinese Academy of Sciences, PO Box 643, Beijing 100044, China*
† Division of Geology, National Museum of Natural Science, Taichung, China

Oviraptorosaurians are an unusual group of theropod dinosaurs, with highly specialized skulls[1–6]. Here we report a new oviraptorosaurian, *Incisivosaurus gauthieri*, gen. et sp. nov., from the lowest part of the Lower Cretaceous Yixian Formation of China. This oviraptorosaurian displays a number of characters closer to more typical theropods, such as a low skull and toothed jaws, thus greatly reducing the morphological gap between oviraptorosaurs and other theropods[4–11]. *Incisivosaurus* has a pair of premaxillary teeth resembling rodent incisors and small, lanceolate cheek teeth with large wear facets. These dental features were previously unknown among theropods and suggest a herbivorous diet. The new discovery provides a case of convergent evolution and demonstrates that non-avian theropods were much more diverse ecologically than previously suspected.

Theropoda Marsh, 1881
Maniraptora Gauthier, 1986
Oviraptorosauria Barsbold, 1976
Incisivosaurus gauthieri gen. et sp. nov.

Holotype. IVPP V13326 (Institute of Vertebrate Paleontology and Paleoanthropology, Beijing), an almost complete skull and a partial cervical vertebra (Fig. 1).

Etymology. The generic name refers to the presence of incisor-like premaxillary teeth; the specific name is in honour of J. Gauthier for his contributions to theropod systematics.

Locality and horizon. Lujiatun, Shangyuan, Beipiao City, Liaoning, China; lowest part of Yixian Formation, older than 128 Myr (ref. 12, Hauterivian).

Diagnosis. An oviraptorosaur displaying the following derived characters: a highly heterodont upper dentition (large incisciform first premaxillary tooth, much smaller, subconical second to fourth premaxillary teeth, and very small lanceolate maxillary teeth); large high-angled wear facets on the mesial margins of the teeth; longitudinal crest on the ventral surface of the basisphenoid; contact between the accessory ventral flanges of the pterygoids; subsidiary ectopterygoid fenestra present; triradiate palatine with very short maxillary process.

Incisivosaurus is a small oviraptorosaur, with a basal skull length of approximately 100 mm. The skull is relatively low, and the length of the snout constitutes 48% of the basal skull length (Fig. 1a). The large, subcircular external naris is positioned high on the snout. A prominent subnarial foramen is visible in lateral view. The oval antorbital fenestra is dorsoventrally tall and anteroposteriorly narrow and the triangular maxillary fenestra is located in the anterior corner of the antorbital fossa. The large orbit is approximately 133% of the antorbital fossa length. The large infratemporal fenestra is subtriangular in outline, and the supratemporal fenestra is long anteroposteriorly. In lateral view, the palate is mostly obscured by the maxilla and jugal; in ventral view, the ventral margins of the premaxillae and maxillae are straight (Fig. 1c), rather than sinuous as in oviraptorids.

The large premaxilla has a shallower main body than that of other oviraptorosaurs[1,2,5,6]. The maxilla forms the anterior border of the antorbital fossa, which contains a pneumatic fossa dorsally and a small opening ventrally between the large antorbital fenestra and the smaller maxillary fenestra. The posteriormost portion of the ventral margin of the maxilla is inset medially, a feature also seen in the troodontid *Sinovenator*[13]. The nasal is pneumatized as in oviraptorids[1], with a large pneumatic fossa immediately posterior to the external naris (Fig. 1a). Unlike other oviraptorosaurs, therizinosaurs, and basal birds[6,14], the nasal is longer than the frontal. The parietal is transversely narrow, and is much shorter than the frontal. The lacrimal is pneumatized, and 'T'-shaped as in dromaeosaurs and troodontids. The postorbital is 'T'-shaped, unlike the condition in other oviraptorosaurs. The quadrate is inclined posterodorsally, and has a pneumatic fossa on the caudal surface at midshaft length (Fig. 1b), as in troodontids[13]. The quadratojugal closely abuts the lateral surface of the quadrate, and is positioned relatively dorsally. The jugal is deep and straplike and is situated below the orbit.

The crescentic occiput has long, pendant paroccipital processes (Fig. 1b), as in oviraptorids[1,15] and a prominent supraoccipital crest. The occipital condyle is smaller than the foramen magnum, which is higher than it is wide. The shallow basisphenoid recess is divided by a longitudinal crest (Fig. 1c). The anteriorly oriented basipterygoid processes are reduced.

The pterygoid has an accessory ventral flange that contacts its fellow on the midline (Fig. 1c). The 'C'-shaped ectopterygoid, with its hooked jugal process, extends vertically. It has an extensive contact with the jugal and barely touches the lacrimal. A large palatine fenestra is present posterior to the palatine, and a second much smaller opening (subsidiary ectopterygoid fenestra) is present between the ectopterygoid and the ventral flange of the pterygoid. The triradiate palatine has a large pterygoid process, a moderately large vomeral process, and a very short maxillary process. The internal naris, usually bordered by the palatine, vomer and maxilla in other non-avian theropods, is absent here; instead, it might be confluent with the subsidiary palatine fenestra that is bordered by the vomer and the vomeral process of the palatine.

The mandible is shallow, with a large, anteroposteriorly long mandibular fenestra (Fig. 1d), as in Caenagnathidae[1–4,16]. The mandibular symphysis is fused, with a small symphyseal shelf. The anterior end of the mandible is toothless and forms a small beak. In side view, the dentary has a slightly convex dorsal margin

